

## Nonstoichiometric Effects in the Leakage Current and Electrical Properties of Bismuth Ferrite Ceramics

Jeong Wook Woo\*, SeungBong Baek\*, Tae Kwon Song\*, Myang Hwan Lee\*, Jamil Ur Rahman\*\*\*, Won-Jeong Kim\*\*\*, Yeon Soo Sung\*\*\*\*, Myong-Ho Kim\*†, and Soonil Lee\*\*\*‡

\*School of Advanced Materials Engineering, Changwon National University, Changwon 51440, Korea

\*\*Energy and Environmental Materials Division, Korea Institute of Ceramic Engineering and Technology, Jinju 52851, Korea

\*\*\*Department of Physics, Changwon National University, Changwon 51140, Korea

\*\*\*\*Department of Materials and Engineering, Pohang University of Science and Technology, Pohang 37673, Korea

(Received May 24, 2017; Revised June 22, 2017; Accepted June 22, 2017)

### ABSTRACT

To understand the defect chemistry of multiferroic BiFeO<sub>3</sub>-based systems, we synthesized nonstoichiometric Bi<sub>1-x</sub>FeO<sub>3+δ</sub> ceramics by conventional solid-state reaction method and studied their structural, dielectric and high-temperature charge transport properties. Incorporation of an excess amount of Bi<sub>2</sub>O<sub>3</sub> lowered the Bi deficiency in BiFeO<sub>3</sub>. Polarization versus electric field (P-E) hysteresis loop and dielectric properties were found to be improved by the Bi<sub>2</sub>O<sub>3</sub> addition. To better understand the defect effects on the multiferroic properties, the high temperature equilibrium electrical conductivity was measured under various oxygen partial pressures (*p*O<sub>2</sub>'s). The charge transport behavior was also examined through thermopower measurement. It was found that the oxygen vacancies contribute to high ionic conduction, showing *p*O<sub>2</sub> independency, and the electronic carrier is electron (*n*-type) in air and Ar gas atmospheres.

**Key words :** Bismuth ferrite, Ferroelectric, Electrical conductivity, Defect, Nonstoichiometry

### 1. Introduction

In February 2003, the Restriction of Hazardous Substances Directive (RoHS) was enacted in Europe and on July 1, 2006, a regulation was enacted restricting the use of lead, cadmium, mercury, hexavalent chrome, phthalates, and brominated flame retardants (PBBs, PBDEs) in electronic products and devices. After such enactments, the usage of lead was regulated, resulting in active research on lead-free (Pb-free) piezoelectric ceramics to replace PZT based materials. Representatively, studies on alkali metal based (Na<sub>0.5</sub>K<sub>0.5</sub>)NbO<sub>3</sub> (NKN), bismuth based (Bi<sub>0.5</sub>Na<sub>0.5</sub>)TiO<sub>3</sub> (BNT) and BiFeO<sub>3</sub> (BFO) compositions are widely being carried out.<sup>1-4</sup> BFO has a rhombohedral (R3c) structure and exhibits multiferroic properties, in which antiferromagnetic and ferroelectric properties coexist at room temperature.<sup>5</sup> Also, BFO has significant advantages of a high Curie temperature (*T*<sub>C</sub>) of 827°C and high Neel temperature (*T*<sub>N</sub>) of 367°C.<sup>6</sup> According to the literature, BFO shows a value of 90 - 100 μC/cm<sup>2</sup> when the spontaneous polarization (*P*<sub>s</sub>) value is orientated in the [111] direction.<sup>7</sup> Despite having

such excellent properties, BFO is known to have limitations in applicability due to its high leakage current. The causes of the leakage current of BFO have been reported to be the combined effect of Bi volatility in the high temperature sintering process and defects of oxygen vacancies due to the transition metal Fe.<sup>8,9</sup> Also, recent reports have shown the effects of secondary phases of BFO like Bi<sub>25</sub>FeO<sub>39</sub> and Bi<sub>2</sub>Fe<sub>4</sub>O<sub>9</sub>, which appear in a specific temperature range (447 - 767°C).<sup>10,11</sup> However, sufficient context is lacking to clearly explain the fundamental cause behind the leakage current due to the significant variation of material properties that result from Bi volatility and Fe transition. In this study, to measure the ferroelectric P-E hysteresis loop, dielectric constant, and dielectric loss at room temperature, and to investigate the leakage current mechanism of BFO, the amount of Bi vulnerable to high temperatures was controlled and nonstoichiometric BFO ceramics of Bi<sub>1-x</sub>FeO<sub>3+δ</sub> were fabricated. Additionally, so that the mechanism behind the main defects and charge transport, which cause the leakage current, could be understood, and in order to identify defects in a specific range, the electrical conductivity and Seebeck coefficient were measured at high temperature with various temperatures and oxygen partial pressures (*p*O<sub>2</sub>).

### 2. Experimental Procedures

In the case of BFO, it is known that fabricating a single phase is difficult due to the volatility and transition issues

†Corresponding author : Myong-Ho Kim

E-mail : mhkim@changwon.ac.kr

Tel : +82-55-213-3711 Fax : +82-55-262-6486

‡Corresponding author : Soonil Lee

E-mail : leesoonil@gmail.com

Tel : +82-55-792-2567 Fax : +82-55-792-2580

of the constituent elements. Single phase BFO can be synthesized when the constituent elements  $\text{Bi}_2\text{O}_3$  and  $\text{Fe}_2\text{O}_3$  have a stoichiometric ratio of exactly 1 : 1. However, since long-term exposure to high temperature is necessary for the ceramic sintering in the fabrication process, it is difficult to evade the temperature range (447 - 767°C) for secondary phase production. In order to overcome this issue, the powder produced after heat treatment was reacted with nitric acid to remove the secondary phase; sol-gel or hydrothermal methods were used to reduce the particle size; or spark plasma sintering (SPS) and rapid sintering were used to reduce the exposure time to the high sintering temperature.<sup>12,13)</sup> However, the above experiment involves cost and environmental issues because acids are used, like nitric acid for the fabrication. Thus, in this study, the general solid-state reaction method was used to prevent the production of the secondary phase after sintering; also, the quenching method was used to rapidly cool to room temperature for BFO ceramic fabrication.

### 2.1. Powder Synthesis and Specimen Preparation

Starting materials  $\text{Bi}_2\text{O}_3$  (Alpha acer 99.99%) and  $\text{Fe}_2\text{O}_3$  (Alpha acer 99.99%), of high purity, were used to fabricate BFO. The mol% values of the starting materials were calculated and weighted according to  $\text{Bi}_{1-x}\text{Fe}_x\text{O}_{3+5}$  ( $x = 0, 0.05$ ). Then, ethanol was used as the solvent, along with the  $\text{ZrO}_2$  balls, to carry out ball milling for 24 h to improve the homogeneity of mixed powder. Afterwards, each specimen was denominated as 0BFO ( $x = 0$ ) and 5BFO ( $x = 0.05$ ). The mixed powder was dried using a dryer and the dried material was heat treated at 700°C under ambient air conditions for 2 h. After the heat treatment, the material was ground in a mortar to improve the powder homogeneity and PVA (polyvinylalcohol) was added to enhance the integration between the powders. The homogeneity of the PVA-added powder was further improved through sieving and the ceramic was fabricated using a uniaxial press.

### 2.2. Sintering Process

Microstructure observation of the BFO ceramic fabricated using the general sintering method (Fig. 1(a)), which performs sintering by raising the temperature to the final sintering temperature in one step, revealed nonuniform grains

and voids here and there.<sup>14,15)</sup> Such voids were observable due to numerous variables including the sintering temperature, sintering time, and heating rate. The two-step sintering method was used to effectively improve such problems in the sintering process.<sup>16)</sup> In order to resolve the reaction issue during high temperature sintering between the  $\text{Al}_2\text{O}_3$  and Bi ion of the BFO, a sufficient amount of BFO powder was applied on an alumina plate to prevent direct reaction between the BFO specimen and  $\text{Al}_2\text{O}_3$ . In addition, in order to prevent Bi ion volatility, which can occur during the high temperature sintering process, sintering was carried out after sufficient application of the BFO powder on the BFO specimen. Also, the temperature of 300°C was maintained for 1 h to remove the PVA in the specimen; then, the temperature was rapidly raised at a rate of 10°C/min to reduce defects that can occur in the secondary phase generation range of 447 - 767°C. Then, after maintaining a temperature of 750°C for 30 minutes, the heating rate was decreased to 2°C/min in order to reduce problems like voids within the ceramic; heating was continued until the final sintering temperature of 820°C. Finally, the temperature of 820°C was maintained for 10 minutes; this was followed by air quenching for rapid cooling until room temperature was reached, so that secondary phase generation during cooling can be prevented. Fig. 1(b) shows the overall two-step sintering process. The structure and crystallinity of the produced specimen were analyzed through XRD (X-ray Diffractometer, Miniflex II, Rigaku); SEM (Scanning Electron Microscope, SEM, JSM-6510) was carried out for microstructural observation.

### 2.3. Electrical Conductivity Measurement

After cutting the  $\text{Bi}_{1-x}\text{Fe}_x\text{O}_{3+5}$  ( $x = 0, 0.05$ ) specimen to dimensions of  $2 \times 2 \times 15 \text{ mm}^3$ , sputtering was used to apply platinum electrodes at regular intervals on the specimen surface. Each of the 4 platinum electrodes was connected to platinum wires and the electrical conductivity was measured for the temperature range of 650 - 750°C. To eliminate the issue of non-ohmic contact, the electrical conductivity was measured using the 4-probe method. The following equation was used to convert the resistance obtained from the specimen measurement to the electrical conductivity.

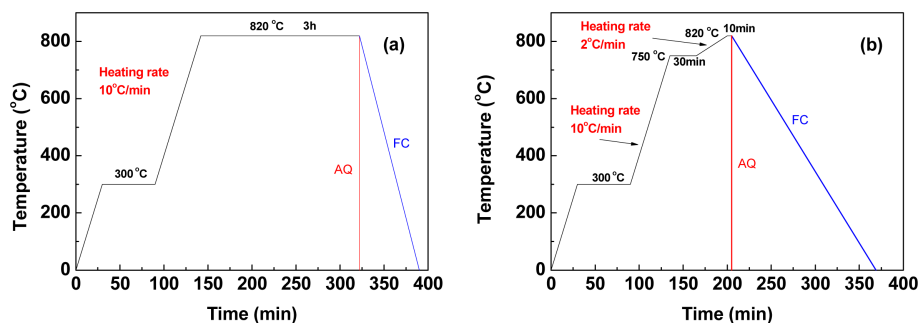
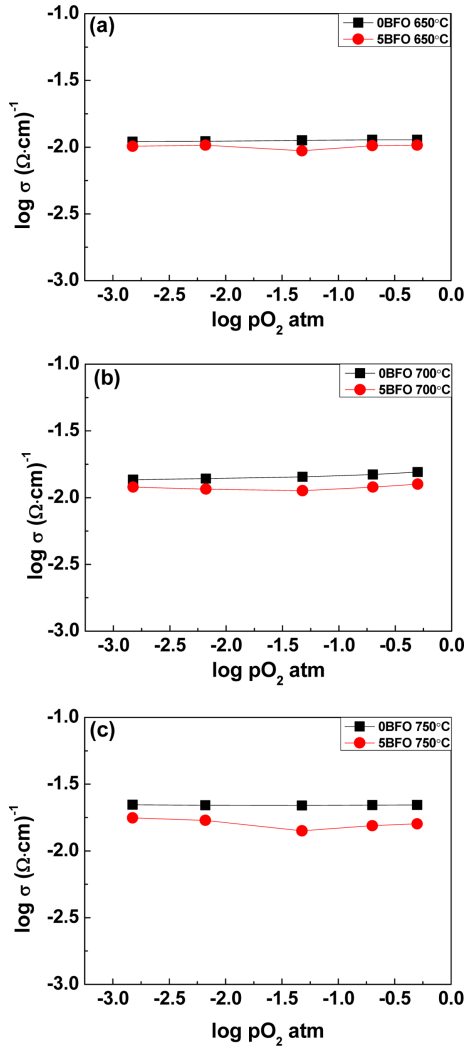


Fig. 1. Conditions for (a) conventional sintering and (b) two-step sintering process; air-quenched (AQ) and furnace-cooled (FC).





**Fig. 5.** Electrical conductivity as a function of oxygen partial pressure ( $pO_2$ ) for 0BFO and 5BFO ceramics at (a) 650°C, (b) 700°C, and (c) 750°C.

various rare earth metals; it shows varying electrical properties. Equivalent impurities that can enter the A-site include  $La^{3+}$ ,  $Nd^{3+}$ , and  $Sm^{3+}$ , while acceptor impurities include  $Ca^{2+}$ ,  $Sr^{2+}$ ,  $Ba^{2+}$ , and  $Pb^{2+}$ . Donor impurities that can enter the B-site include  $V^{5+}$ ,  $Nb^{5+}$ ,  $Mn^{4+}$ , and  $Ti^{4+}$ .<sup>17-20)</sup> Additionally, BFO can have oxygen vacancy defects due to Bi volatility and Fe electrovalence transition. In this study, the electrical properties of pure BFO were investigated.

Figure 5 shows the electrical conductivity measurement results for 0BFO and 5BFO. Fig. 6 provides a diagram of the electrical property based on the defects in BFO. Compared to this, no variation of the electrical conductivity as a function of the oxygen partial pressures ( $pO_2$ ) can be observed in Fig. 5(a) - (c). This behavior suggests that the ionic conductivity is higher than the electronic conductivity within the BFO. This can be explained through the following reaction formula.

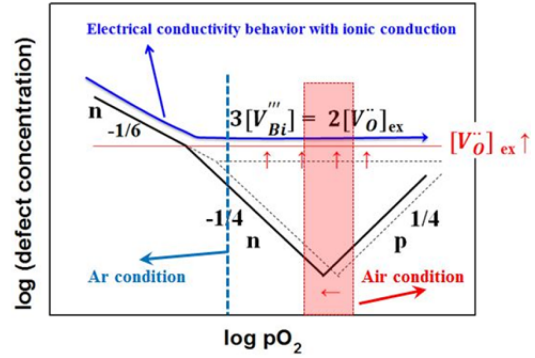
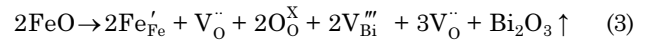
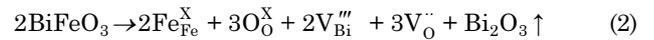


**Fig. 6.** Schematic diagram of defect concentration (electrical conductivity) vs. oxygen partial pressure ( $pO_2$ ).



Equation (2) is the reaction formula for Bi volatility; Eq. (3) is the reaction formula for Fe transition, incorporating Eqs. (2) and (4). Thus, it can be explained that the ionic conductivity by oxygen vacancy ( $V_O''$ ) is dominant due to oxygen vacancy compensation for Bi volatility or transition of Fe from  $Fe^{3+}$  to  $Fe^{2+}$ . For the latter case of Fe transition (Eq. (3)), the dominant defect reacts according to Eq. (2) because the latter case is derived from oxygen vacancy due to Bi volatility. Eqs. (4) and (5) are the reaction formula for each of the oxidation and reduction reactions; the above 4 types of defects coexist in a manifold manner. The dominant defect reaction differs according to the degree of oxygen vacancy and the degree of Bi volatility (or Bi content). Figs. 5(a) - (c) show that the electrical conductivity value ( $\log \sigma$ ) for 5BFO was lower than that for 0BFO. This difference was thought to indicate a decrease in the overall electrical conductivity ( $\sigma_{total} = \sigma_{ion} + \sigma_{electronic}$ ) as the ionic conductivity ( $\sigma_{ion}$ ) decreased due to the decreased oxygen vacancy concentration as the Bi volatility amount was compensated for with the 5% excess Bi in the sintering process. This type of ionic conductivity phenomenon was in agreement with the results of Yeo *et al.*<sup>21)</sup> but in contrast to the reported  $n$ - $p$  transition behavior with dominant electron/hole conduction, as reported by Rojac *et al.*<sup>22)</sup> This shows that ionic conduction overwhelming electronic conductivity ( $\sigma_{electronic}$ ) can occur sufficiently with Bi volatility because the electrical conductivity difference is due to the difference in the actual nonstoichiometry in the fabrication of pure BFO. Evidence of the ionic conductivity was also observed in the dielectric loss measurement results, which will be shown later.

Figure 7 shows the activation energy ( $E_a$ ) for electrical conduction obtained for each specimen on an Arrhenius

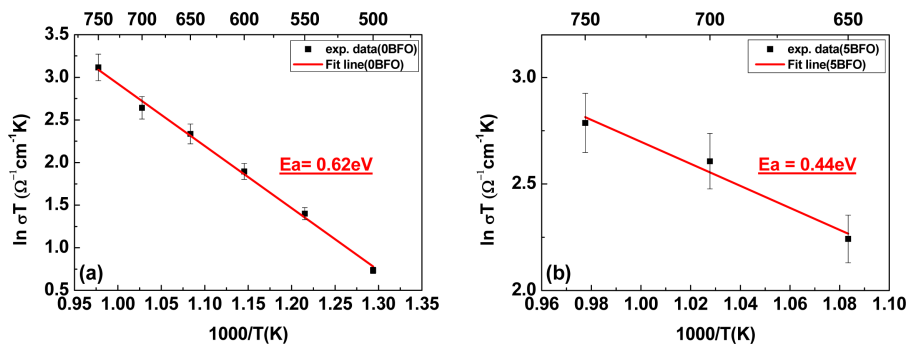


Fig. 7. Arrhenius plots of electrical conductivity for air-quenched (AQ) (a) 0BFO and (b) 5BFO.

plot. The slopes of the Arrhenius plot were used to calculate the activation energy through the below equation.

$$\ln \sigma T \propto -\frac{E_a}{k_B T} \quad (6)$$

The activation energy values of 0BFO (Fig. 7(a)) and 5BFO (Fig. 7(b)) were 0.62 and 0.44 eV, respectively. These values are within the 0.4 - 1.0 eV activation energy range for oxygen vacancy movement for typical  $ABO_3$ ,<sup>23-25)</sup> thus, all the obtained activation energy results showed ionic conductivity behavior due to oxygen vacancy.

### 3.3. Seebeck Coefficient

In order to investigate the types of charge carriers, the Seebeck coefficient of 0BFO was measured as shown in Fig. 8. The measurements were conducted for in air and Ar gas atmospheres and a temperature range of 200 - 500°C. The Seebeck coefficient represents the thermoelectric power of the electron/hole carrier rather than that of the ion carrier. As shown in the oxygen partial pressure and electrical conductivity diagram of Fig. 6, the contribution of ionic conductivity was high in the measured oxygen partial pressure regime, and so the overall electrical conductivity was a constant value regardless of the oxygen partial pressure. However, minor carriers with low contribution actually coexist within the material and electron/hole conductivity transition ( $n$ - $p$  transition) behavior was observed for the oxygen partial pressure of this regime. Such  $n$ - $p$  transition was also easily observed in the results of Rojac *et al.*,<sup>19)</sup> which showed dominant electron/hole conductivity due to low oxygen vacancy concentration. In this study, the oxygen vacancy concentration for the measured 0BFO is relatively high, and so the  $n$ - $p$  transition regime moves towards the low oxygen partial pressure because the ionic conduction by the oxygen vacancies is dominant. This movement of the  $n$ - $p$  transition regime is also observed with temperature decrease. Thus, although the Seebeck coefficient measured in air atmosphere had a positive value ( $p$ -type) at low temperature, the Seebeck coefficient became negative or of  $n$ -type with temperature increase. A decrease in the absolute value of the Seebeck coefficient means that the charge carrier concentration increased. The relationship between the charge carrier

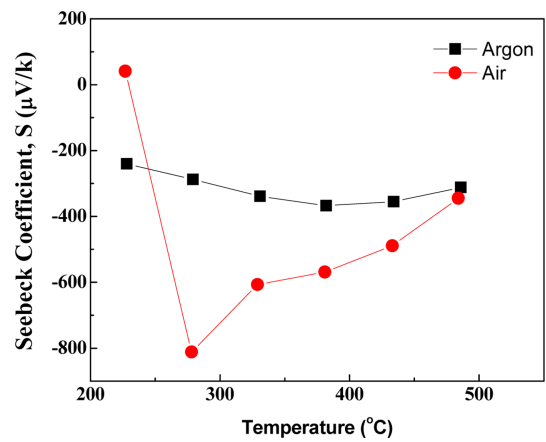


Fig. 8. Seebeck coefficient ( $S$ ) vs. temperature for 0BFO in different atmospheres (Argon and air).

concentration ( $n$ ) and Seebeck coefficient ( $S$ ) can be expressed by the Pisarenko expression, given in Eq. (7).<sup>26)</sup>

$$S = \frac{8\pi^2 k_B^2}{3eh^2} \left(\frac{\pi}{3n}\right)^{2/3} m_d^* T \quad (7)$$

Here,  $k_B$  is the Boltzmann constant,  $h$  is the Planck constant, and  $m_d^*$  is the density of state (DOS) effective mass. The Seebeck coefficient ( $S$ ) is inversely proportional to the charge carrier concentration ( $n$ ). The Seebeck coefficient was a negative value or was of  $n$ -type for the Ar gas atmosphere. The absolute value of the Seebeck coefficient was smaller than that of the air atmosphere; this signifies the increase of the electron concentration in the Ar gas atmosphere, as shown in Eq. (7) and Fig. 6.

### 3.4. P-E Hysteresis Loop

Figure 9 shows the P-E hysteresis loop measurement results for 0BFO and 5BFO. The measurement results show that the remnant polarization ( $P_r$ ) values for 0BFO and 5BFO were 91  $\mu\text{C}/\text{cm}^2$  and 83  $\mu\text{C}/\text{cm}^2$ , respectively. These values were similar to the typical value of 90 - 100  $\mu\text{C}/\text{cm}^2$  for BFO (single crystal). However, it is anticipated that the absence of complete saturation in the P-E hysteresis loop means that the hysteresis loop do not show capacitance but

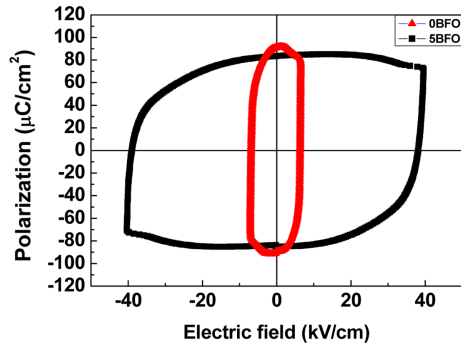


Fig. 9. Room temperature ferroelectric hysteresis ( $P$ - $E$ ) loops of air-quenched (AQ) 0BFO and 5BFO.

rather behavior due to current within the material or leakage current amount. The reason behind the low polarization value for 5BFO was thought to be the decrease in the leakage current compared to that of 0BFO due to the oxygen vacancy concentration decrease from excess Bi. Observation of the coercive field also revealed that the coercive field of 5BFO was greater than that of 0BFO. This proves the idea that the dielectric loss of 5BFO is small.

### 3.5. Dielectric Constant and Dielectric Loss Measurement

Figure 10 shows the values of dielectric constant and dielectric loss of 0BFO and 5BFO. The measured dielectric constants shown in Figs. 10(a) and (c) indicate that the

dielectric constant decreased as the measuring frequency (1, 10, 100 kHz) increased and the emerging Neel temperature ( $T_N$ ) range increased as the frequency increased. This frequency dependency clearly shows multiferroicity. The dielectric losses shown in Figs. 10(b) and (d) reveal large dielectric loss values starting from the low temperature range; the dielectric loss value for 0BFO, shown in Fig. 10(b), rapidly increased starting at a temperature lower than was the case for 5BFO, as shown in Fig. 10(d). This shows that dielectric loss occurs easily due to the higher oxygen vacancy concentration, which was compensated for Bi vacancy, of 0BFO compared to that of 5BFO. The high dielectric loss for BFO at a specific temperature and the lower frequency was in good agreement with the high ionic conductivity in the high temperature electrical conductivity results. This clearly shows that the oxygen vacancy concentration of BFO is high and transport is also high.

## 4. Conclusions

In this study, the microstructure, electrical conductivity, and  $P$ - $E$  hysteresis curve were investigated for  $X = (0, 0.05)$   $\text{Bi}_{1-x}\text{FeO}_{3\pm\delta}$  ceramics at various oxygen partial pressure atmospheres. The 0BFO and 5BFO ceramics were synthesized using the solid-state reaction method; to improve the microstructure and porosity, the synthesized ceramics were sintered using the two-step sintering method. High temperature electrical conductivity was measured to assess the main defect behavior of BFO. The high ionic conductivity

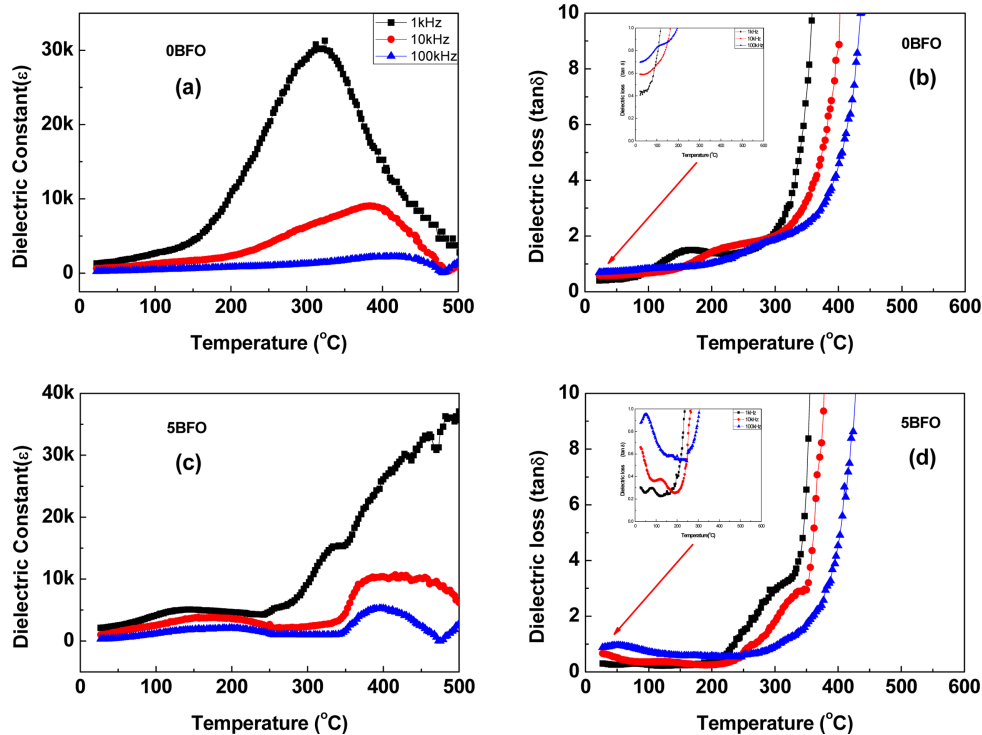


Fig. 10. Temperature dependence of dielectric constant ( $\epsilon$ ) (a, c) and dielectric loss ( $\tan\delta$ ) (b, d) for the air-quenched (AQ) 0BFO and 5BFO with measurement frequency from 1 kHz to 100 kHz.

due to oxygen vacancy compensation reaction ( $3[V_{\text{Bi}}^{\prime\prime}] \approx 2[V_{\text{O}}^{\bullet\bullet}]$ ), resulting from the Bi volatility, and thereby oxygen vacancy compensation reaction ( $[Fe_{\text{Fe}}^{\prime}] \approx 2[V_{\text{O}}^{\bullet\bullet}]$ ) by the Fe electrovalence transition, was identified. With those oxygen vacancies, BFO was found to have a high leakage current. Volatile Bi during sintering was compensated for by excess Bi, and thereby there was a reduction of the oxygen vacancy concentration, which decreased the overall electrical conductivity due to the resulting ionic conductivity decrease. Such ionic conductivity was also observed in the activation energy results of 0.62 and 0.44 eV. Although the ionic conductivity is dominant, the minor charge carrier was found to be of  $n$ -type, with a negative Seebeck coefficient value. The polarization values of  $91 \mu\text{C}/\text{cm}^2$  and  $83 \mu\text{C}/\text{cm}^2$  were within the typical BFO range of  $90 - 100 \mu\text{C}/\text{cm}^2$ , but the P-E hysteresis curve showed high leakage current by oxygen vacancies. Furthermore, the high dielectric loss and its frequency dependence clearly showed the characteristic of leakage current due to oxygen vacancy.

### Acknowledgements

This work was supported by the basic research program through the National Research Foundation of Korea (NRF), funded by Ministry of Education, Science and Technology (MEST) (2011-0030058) and the National Research Foundation of Korea (NRF-2015R1D1A1A01061479).

### REFERENCES

1. M. H. Lee, D. J. Kim, J. S. Park, S. W. Kim, T. K. Song, M.-H. Kim, W.-J. Kim, D. Do, and I.-K. Jeong, "High-Performance Lead-Free Piezoceramics with High Curie Temperatures," *Adv. Mater.*, **27** [43] 6976-82 (2015).
2. K. T. Lee, J. S. Park, J. H. Cho, Y. H. Jeong, J. H. Paik, and J. S. Yun, "The Study on the Phase Transition and Piezoelectric Properties of  $\text{Bi}_{0.5}(\text{Na}_{0.78}\text{K}_{0.22})_{0.5}\text{TiO}_3$ - $\text{LaMnO}_3$  Lead-Free Piezoelectric Ceramics," *J. Korean Ceram. Soc.*, **52** [4] 237-42 (2015).
3. J. Kim, I. Seo, J. Hur, D. Kim, and S. Nahm, "Effect of  $\text{MnO}_2$  Addition on Microstructure and Piezoelectric Properties of  $0.95(\text{Na}_{0.5}\text{K}_{0.5})\text{NbO}_3$ - $0.05\text{CaTiO}_3$  Piezoelectric Ceramics," *J. Korean Ceram. Soc.*, **53** [2] 129-33 (2016).
4. H. Han, I. Hong, Y. Kong, J. Lee, and W. Jo, "Effect of Nb Doping on the Dielectric and Strain Properties of Lead-free  $0.94(\text{Bi}_{1/2}\text{Na}_{1/2})\text{TiO}_3$ - $0.06\text{BaTiO}_3$  Ceramics," *J. Korean Ceram. Soc.*, **53** [2] 145-49 (2016).
5. L. W. Martin, S. P. Crane, Y.-H. Chu, M. B. Holcomb, M. Gajek, M. Huijben, N. Balke, and R. Ramesh, "Multiferroics and Magnetoelectrics: Thin Films and Nanostructures," *J. Phys.: Condens. Matter.*, **20** [43] 434220 (2008).
6. X.-Z. Chen, R.-L. Yang, J.-P. Zhou, X.-M. Chen, Q. Jiang, and P. Liu, "Dielectric and Magnetic Properties of Multiferroic  $\text{BiFeO}_3$  Ceramics Sintered with the Powders Prepared by Hydrothermal Method," *Solid State Sci.*, **19** 117-21 (2013).
7. J. B. Neaton, C. Ederer, U. V. Waghmare, N. A. Spaldin, and K. M. Rabe, "First-Principles Study of Spontaneous Polarization in Multiferroic  $\text{BiFeO}_3$ ," *Phys. Rev. B*, **71** [1] 014113 (2005).
8. Z. Zhang, P. Wu, L. Chen, and J. Wang, "Density Functional Theory Plus U Study of Vacancy Formations in Bismuth Ferrite," *Appl. Phys. Lett.*, **96** [23] 232906 (2010).
9. S. Guilin, S. Jian, N. Zhang, and C. Fanggao, "Effects of Oxygen Content on the Electric and Magnetic Properties of  $\text{BiFeO}_3$  Compound," *Phys. B*, **493** 47-52 (2016).
10. S. M. Selbach, M.-A. Einarsrud, and T. Grande, "On the Thermodynamic Stability of  $\text{BiFeO}_3$ ," *Chem. Mater.*, **21** [1] 169-73 (2009).
11. S. M. Selbach, T. Tybell, M.-A. Einarsrud, and T. Grande, "Phase Transitions, Electrical Conductivity and Chemical Stability of  $\text{BiFeO}_3$  at High Temperatures," *J. Solid State Chem.*, **183** [5] 1205-8 (2010).
12. Z. Dai and Y. Akishige, "Electrical Properties of Multiferroic  $\text{BiFeO}_3$  Ceramics Synthesized by Spark Plasma Sintering," *J. Phys. D: Appl. Phys.*, **43** [44] 445403 (2010).
13. A. Perejón, N. Masó, A. R. West, P. E. Sánchez-Jiménez, R. Poyato, J. M. Criado, and L. A. Pérez-Maqueda, "Electrical Properties of Stoichiometric  $\text{BiFeO}_3$  Prepared by Mechanochemical Synthesis with Either Conventional or Spark Plasma Sintering," *J. Am. Ceram. Soc.*, **96** [4] 1220-27 (2013).
14. N. Jeon, K.-S. Moon, D. Rout, and S.-J. L. Kang, "Enhanced Sintering Behavior and Electrical Properties of Single Phase  $\text{BiFeO}_3$  Prepared by Attrition Milling and Conventional Sintering," *J. Korean Ceram. Soc.*, **49** [6] 485-92 (2012).
15. D. Rout, K.-S. Moon, and S.-J. L. Kang, "Temperature-Dependent Raman Scattering Studies of Polycrystalline  $\text{BiFeO}_3$  Bulk Ceramics," *J. Raman Spectrosc.*, **40** [6] 618-26 (2009).
16. R.-Q. Yin, B.-W. Dai, P. Zheng, J.-J. Zhou, W.-F. Bai, F. Wen, J.-X. Deng, L. Zheng, J. Du, and H.-B. Qin, "Pure-Phase  $\text{BiFeO}_3$  Ceramics with Enhanced Electrical Properties Prepared by Two-Step Sintering," *Ceram. Int.*, **43** [8] 6467-71 (2017).
17. N. Masó and A. R. West, "Electrical Properties of Ca-Doped  $\text{BiFeO}_3$  Ceramics: From  $p$ -Type Semiconduction to Oxide-Ion Conduction," *Chem. Mater.*, **24** [11] 2127-32 (2012).
18. G. Arya, R. K. Kotnala, and N. S. Negi, "A Novel Approach to Improve Properties of  $\text{BiFeO}_3$  Nanomultiferroics," *J. Am. Ceram. Soc.*, **97** [5] 1475-80 (2014).
19. J. Wei, Y. Liu, X. Bai, C. Li, Y. Liu, Z. Xu, P. Gemeiner, R. Haumont, I. C. Infante, and B. Dkhil, "Crystal Structure, Leakage Conduction Mechanism Evolution and Enhanced Multiferroic Properties in Y-doped  $\text{BiFeO}_3$  Ceramics," *Ceram. Int.*, **42** [12] 13395-403 (2016).
20. K. Abe, N. Sakai, J. Takahashi, H. Itoh, N. Adachi, and T. Ota, "Leakage Current Properties of Cation-Substituted  $\text{BiFeO}_3$  Ceramics," *Jpn. J. Appl. Phys.*, **49** [9S] 09MB01 (2010).
21. H.-G. Yeo, T.-K. Song, Y.-S. Sung, J.-H. Cho, H.-M. Lee, and M.-H. Kim, "Effects of Nb Substitution on the Leakage Currents and the Electrical Properties of Ceramics," *New Phys.: Sae Mulli.*, **56** [3] 278-82 (2008).

22. T. Rojac, A. Bencan, B. Malic, G. Tutuncu, J. L. Jones, J. E. Daniels, and D. Damjanovic, "BiFeO<sub>3</sub> Ceramics: Processing, Electrical, Electromechanical Properties," *J. Am. Ceram. Soc.*, **97** [7] 1993-2011 (2014).
23. S. J. Clacrk and J. Robertson, "Energy Levels of Oxygen Vacancies in BiFeO<sub>3</sub> by Screened Exchange," *Appl. Phys. Lett.*, **94** [2] 022902 (2009).
24. H.-Y. Su and K. Sun, "DFT Study of Stability of Oxygen Vacancy in Cubic ABO<sub>3</sub> Perovskites," *J. Mater. Sci.*, **50** [4] 1701-9 (2015).
25. W. L. Warren, K. Vanheusden, D. Dimos, G. E. Pike, and B. A. Tuttle, "Oxygen Vacancy Motion in Perovskite Oxides," *J. Am. Ceram. Soc.*, **79** [2] 536-38 (1996).
26. G. J. Snyder and E. S. Toberer, "Complex Thermoelectric Materials," *Nat. Mater.*, **7** [2] 105-14 (2008).